Journal of
Materials Chemistry A

ROYAL SOCIETY
OF CHEMISTRY

PAPER

View Article Online
View Journal

Cite this: DOI: 10.1039/d5ta04422g

Electrospun bilayered PVDF-HFP-TiO_2/Al_2O_3 nanofiber membranes for high-performance passive radiative cooling

Dhandayuthapani Thiyagarajan, †[a] Shichen Li†[a] and Bong-Kee Lee *[ab]

Passive radiative cooling is an emerging strategy for reducing heat accumulation by efficiently reflecting solar radiation and emitting thermal energy within the atmospheric transparency window (8–13 μm). In this study, we systematically compared four architectural designs for radiative cooling membranes: PVDF-HFP-TiO_2, PVDF-HFP-Al_2O_3, a mixed PVDF-HFP-TiO_2-Al_2O_3 composite, and bilayered PVDF-HFP-TiO_2/Al_2O_3. The incorporation of strategically sized TiO_2 (0.7–1.1 μm) and Al_2O_3 (50–300 nm) microspheres was found to enhance broadband solar reflectance *via* complementary Mie scattering, with TiO_2 primarily scattering near-infrared light and Al_2O_3 effectively scattering visible radiation. While all the samples exhibited high solar reflectance (~90–95%) and strong mid-infrared emissivity (~0.98), bilayered PVDF-HFP-TiO_2/Al_2O_3 demonstrated superior cooling, achieving a temperature reduction of 12 °C compared to only 9 °C for pure Al_2O_3, 10 °C for the mixed composite, and 8 °C for pure TiO_2. Theoretical analysis using a mid-latitude summer atmospheric model predicted a cooling power of 71.7 W m^{-2} and 121.7 W m^{-2} for the bilayered membrane during the day and at night, respectively, validating the experimental results. This structural advantage arises from the strategic segregation of optical functions into distinct layers, thus optimizing solar reflection and thermal emission while minimizing particle interference effects. The bilayered membrane exhibited excellent thermal stability, hydrophobic properties, and mechanical integrity, making it a promising candidate for energy-efficient cooling applications in buildings, textiles, and outdoor electronics.

Received 2nd June 2025
Accepted 7th August 2025

DOI: 10.1039/d5ta04422g

rsc.li/materials-a

1. Introduction

Climate change and global warming have prompted the search for more sustainable thermal management technologies that minimize energy consumption and environmental impacts. Conventional cooling systems, such as compression-based air conditioning and evaporative cooling systems, are major contributors to global energy consumption and greenhouse gas emissions.[1,2] Accordingly, passive radiative cooling has emerged as a promising alternative that effectively dissipates heat without requiring any electricity input. This technology exploits the atmospheric transparency window (8–13 μm) to emit terrestrial heat directly into cold outer space while simultaneously reflecting incoming solar radiation (300–2500 nm).[3,4] Materials that are capable of both solar reflection and thermal emission can achieve sub-ambient cooling without energy consumption, thus they hold great promise for use in sustainable building design and personal thermal management.[5,6]

Recent research in radiative cooling has explored various materials and structures, including polymeric matrices, photonic architectures, and biomimetic designs.[7–12] Polymeric materials, such as polyacrylonitrile (PAN), polyvinylidene fluoride (PVDF), polyethylene (PE), and cellulose acetate (CA), have gained particular attention because of their intrinsic mid-infrared emission properties and processability.[7–10] These materials have also been modified by incorporating metal oxides, and MXenes into their polymer matrices using a variety of fabrication approaches.[10–13] In particular, the electrospinning of polymer nanofibers offers distinct advantages, including high porosity, tunable morphology, and scalable production capabilities, which are essential for practical applications.[13–15]

Despite their promising optical properties, polymer-based radiative cooling materials are often limited by their poor environmental durability. Many polymers degrade with prolonged exposure to solar radiation, moisture, and temperature fluctuations, which limits their long-term performance in outdoor settings. To address this, researchers have incorporated metal oxide particles such as TiO_2, Al_2O_3, and SiO_2 into polymer matrices.[16–22] These particles not only enhance solar reflectance through Mie scattering but also improve the thermal and mechanical stability of the composite materials.[21–26] However, optimizing the composition, particle size, and

---

[a] *School of Mechanical Engineering, Chonnam National University, 77 Yongbong-ro, Buk-gu, Gwangju, 61186, Republic of Korea. E-mail: b.lee@chonnam.ac.kr*

[b] *Faculty of Mechanical Engineering, Industrial University of Ho Chi Minh City, 12 Nguyen Van Bao, Ward 4, Go Vap District, Ho Chi Minh City, 71408, Vietnam*

† These authors contributed equally to this work.

structural arrangement of these components remains difficult because excessive particle loads can compromise the mechanical integrity and optical performance of the polymer matrix due to phase segregation and agglomeration.

In the present study, we compared four architectural designs for radiative cooling membranes based on the polymer poly(vinylidene fluoride-*co*-hexafluoropropylene) (PVDF-HFP) and metal oxide particles. The first design was a single-layered PVDF-HFP-TiO_2 structure in which TiO_2 microspheres (0.7–1.1 μm) provide near-infrared scattering while the PVDF-HFP matrix generates mid-infrared emission *via* C–F vibrational modes. The second structure was a single-layered PVDF-HFP-Al_2O_3, with Al_2O_3 microspheres (50–300 nm) inducing efficient visible and short-wavelength NIR scattering for high solar reflectance. The third structure was a mixed PVDF-HFP-TiO_2-Al_2O_3 composite, which combines the complementary scattering properties of Al_2O_3 (visible light scattering) and TiO_2 (NIR scattering) to achieve broadband solar reflection. The fourth design employed a bilayered PVDF-HFP-TiO_2/Al_2O_3 structure with a PVDF-HFP-Al_2O_3 top layer (75 μm) optimized for visible/short-wavelength NIR reflection and a PVDF-HFP-TiO_2 bottom layer (75 μm) designed for long-wavelength NIR management and enhanced thermal emission. The bilayered architecture facilitates the strategic segregation of optical functions into distinct layers, optimizing both solar reflection and thermal emission while minimizing the constraints imposed by combining these functions into a single layer. We systematically evaluated these four designs based on their structural, thermal, and optical properties, and assessed their outdoor cooling performance under various environmental conditions. This comparative analysis provided insights into the structure–property relationships governing radiative cooling efficiency, guiding the design of next-generation cooling materials for building envelopes, textiles, and electronic devices. Our approach focuses on scalable fabrication methods and environmentally robust materials to facilitate the practical implementation of passive radiative cooling technology.

2. Experimental section

2.1 Materials

PVDF-HFP (molecular weight [MW]: 400 000), titanium isopropoxide ($C_{12}H_{28}O_4Ti$; MW: 284.22), acetone (CH_3COCH_3; MW: 58.08), and dimethylformamide ($HCON(CH_3)_2$; MW: 73.09) were all of analytical grade and obtained from Sigma-Aldrich. Al_2O_3 microparticles were purchased from Ditto Technologies, South Korea, and used as received without further purification.

2.2 Preparation of rutile TiO_2 microspheres

TiO_2 microspheres were synthesized using a previously reported method with modifications.[27] The as-prepared TiO_2 samples were calcined at 700 °C for 2 h in an air atmosphere to obtain rutile-phase TiO_2 microspheres. These rutile TiO_2 microspheres were subsequently used in the fabrication of PVDF-HFP-TiO_2, PVDF-HFP-TiO_2-Al_2O_3, and PVDF-HFP-TiO_2/Al_2O_3 nanofibers.

2.3 Preparation of PVDF-HFP-TiO_2, PVDF-HFP-Al_2O_3, PVDF-HFP-TiO_2-Al_2O_3, and PVDF-HFP-TiO_2/Al_2O_3 nanofibers

PVDF-HFP-TiO_2 and PVDF-HFP-Al_2O_3 nanofibers were prepared by separately dispersing 20 wt% of the respective microspheres (TiO_2 and Al_2O_3) into a PVDF-HFP electrospinning solution and stirring the mixture continuously for 8 h. Nanofiber-based fabric was then fabricated using an electrospinning machine at 18 kV with a feeding rate of 0.5 mL h^{-1}. The PVDF-HFP-TiO_2-Al_2O_3 layer was prepared in a similar manner by incorporating 10 wt% TiO_2 and 10 wt% Al_2O_3 into the PVDF-HFP solution before electrospinning. The PVDF-HFP-TiO_2-Al_2O_3 mixed composite nanofiber is referred to as PVDF-HFP-Ti-Al in all figures throughout the manuscript. For the bilayered structure, a PVDF-HFP-TiO_2 nanofiber layer (75 μm thick) was fabricated as previously described, and then a PVDF-HFP-Al_2O_3 layer (75 μm thick, 20 wt% Al_2O_3 concentration) was directly electrospun on top. The total thickness of all prepared nanofiber fabrics was approximately 150 μm.

3. Results and discussion

3.1 Structural design and characterization

Generally, a passive radiative cooling membrane must exhibit high solar reflectance and broadband thermal emittance within the 8–13 μm atmospheric window. In this study, PVDF-HFP was chosen as the polymer matrix because of its strong mid-infrared emission, which is attributed to its C–F ($\sim$1140–1210 cm^{-1}) and C–H vibrational bonds, which enhance thermal radiation in the atmospheric window.[28–30] This strong mid-infrared emission capability makes it a key component for radiative cooling.[31] Additionally, PVDF-HFP provides excellent mechanical and thermal stability, making it ideal for outdoor applications. To achieve broadband solar reflection, TiO_2 and Al_2O_3 microparticles were incorporated because of their high refractive indices and distinct scattering properties. Although TiO_2 efficiently scatters visible light, it primarily absorbs UV light rather than reflecting it. Conversely, Al_2O_3 provides strong NIR scattering. Collectively, they enhance solar reflectance across the 400–2500 nm range. The preparation process for the PVDF-HFP-TiO_2/Al_2O_3 nanofibers is presented in Fig. 1(a). Field-emission scanning electron microscopy (FE-SEM) images and the average diameter distribution of PVDF-HFP, TiO_2, and Al_2O_3 are presented in Figs. S1 and S2.

The surface morphology of the prepared PVDF-HFP-TiO_2, PVDF-HFP-Al_2O_3, PVDF-HFP-TiO_2-Al_2O_3, and PVDF-HFP-TiO_2/Al_2O_3 nanofibers is presented in Fig. 1(b)–(e). The PVDF-HFP-TiO_2 nanofiber membrane exhibited a smooth and continuous fiber morphology. The rutile TiO_2 microspheres were embedded within the fibers, forming bulging node-like structures that enhance light scattering through refractive index contrast and surface roughness. The PVDF-HFP-Al_2O_3 nanofibers had Al_2O_3 microspheres of various sizes randomly distributed on their surface. In the PVDF-HFP-TiO_2-Al_2O_3 nanofibers, the small Al_2O_3 microspheres were dispersed across the fiber surface with a more uniform distribution, which enhances broadband solar reflection. In contrast, the PVDF-HFP-TiO_2/Al_2O_3 nanofiber

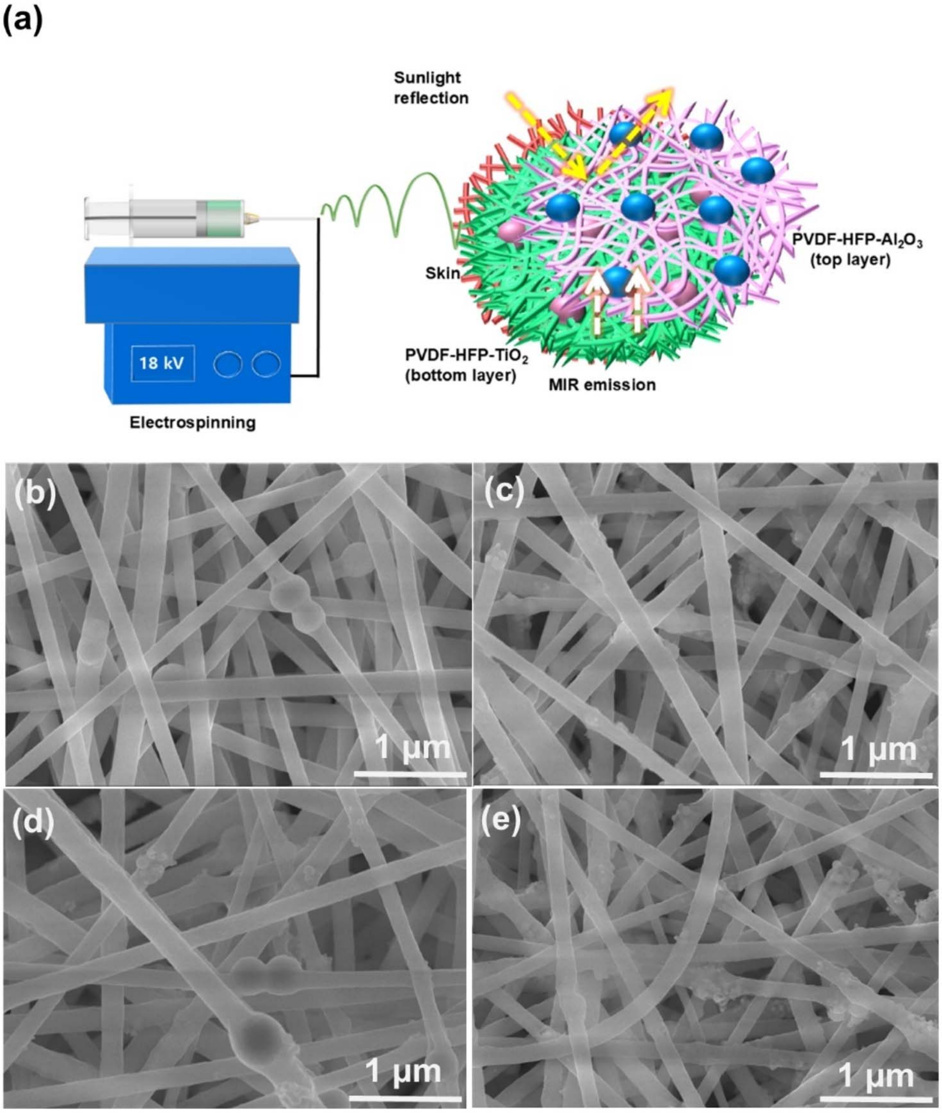

Fig. 1 (a) Schematic illustration of the preparation of the PVDF-HFP-TiO_2/Al_2O_3 nanofibers. FE-SEM images of (b) PVDF-HFP-TiO_2 and (c) PVDF-HFP-Al_2O_3, (d) PVDF-HFP-TiO_2-Al_2O_3, and (e) PVDF-HFP-TiO_2/Al_2O_3 nanofibers.

membrane exhibited a heterogeneous interwoven nanofiber network. In this network, the Al_2O_3 microspheres were embedded within the nanofibers at the top, while the TiO_2-embedded nanofibers at the bottom merged, creating an interconnected architecture that optimizes light scattering and structural complexity while maximizing solar reflection and thermal emissivity. The elemental mapping images of the top, bottom layers of the PVDF-HFP-TiO_2/Al_2O_3 and PVDF-HFP-TiO_2-Al_2O_3 (mixed composite) nanofibers are presented in Fig. S3–S5. The elemental composition results confirmed the presence of titanium and aluminum in the nanofiber matrix.

X-ray diffraction (XRD) patterns of the rutile TiO_2, α-Al_2O_3, PVDF-HFP-TiO_2, PVDF-HFP-TiO_2-Al_2O_3, and PVDF-HFP-TiO_2/Al_2O_3 nanofibers are presented in Fig. 2(a). The strong diffraction peak at ∼27.4° in the PVDF-HFP-TiO_2, PVDF-HFP-TiO_2-Al_2O_3, and PVDF-HFP-TiO_2/Al_2O_3 nanofibers corresponded to the (110) plane of rutile TiO_2 (JCPDS No. 21-1276), confirming the successful incorporation of rutile TiO_2 into the polymer matrix. The distinct diffraction peaks at ∼32.6° and ∼36.7° in the PVDF-HFP-TiO_2-Al_2O_3 and PVDF-HFP-TiO_2/Al_2O_3 nanofibers corresponded to the (113) and (202) planes of α-Al_2O_3 (corundum phase, JCPDS No. 46-1212), supporting the inclusion of α-Al_2O_3 microspheres in the composite fibers.[32,33] Diffraction peaks for pure TiO_2 and α-Al_2O_3 were observed in the composite nanofibers, confirming the presence of both crystalline phases. The XRD patterns of the PVDF-HFP-TiO_2 and PVDF-HFP-TiO_2-Al_2O_3 nanofibers also displayed broad diffraction backgrounds, indicating the presence of an amorphous polymer matrix, while retaining the characteristic peaks of TiO_2 and α-Al_2O_3.

Thermogravimetric analysis (TGA) curves for the PVDF-HFP-TiO_2, PVDF-HFP-TiO_2-Al_2O_3, and PVDF-HFP-TiO_2/Al_2O_3 nanofibers are displayed in Fig. 2(b). All of the samples exhibited minimal weight loss below 300 °C, indicating the absence of

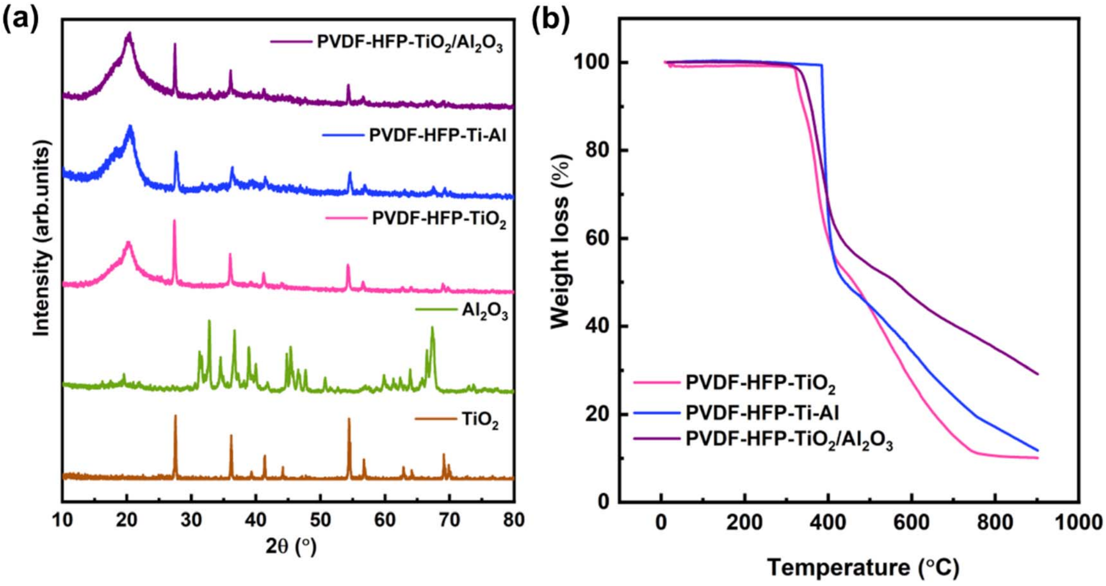

Fig. 2 (a) XRD patterns and (b) TGA curves for the PVDF-HFP-TiO_2, PVDF-HFP-TiO_2-Al_2O_3, and PVDF-HFP-TiO_2/Al_2O_3 nanofibers.

significant volatile degradation. A major degree of decomposition occurred at 400–500 °C due to the thermal breakdown of the PVDF-HFP polymer matrix. The PVDF-HFP-TiO_2 nanofiber membrane degraded more rapidly, while the PVDF-HFP-TiO_2-Al_2O_3 and PVDF-HFP-TiO_2/Al_2O_3 nanofibers exhibited a delayed onset of weight loss, suggesting enhanced thermal stability due to Al_2O_3 incorporation.

3.2 Optical characterization

The morphology and size distribution of the Al_2O_3 and TiO_2 microspheres were examined using FE-SEM imaging and statistical particle size analysis (Fig. S2). The SEM micrograph of the Al_2O_3 particles revealed a heterogeneous distribution of microspheres with particle sizes ranging from ~50 nm to 300 nm, which was confirmed by the particle size distribution histogram. In contrast, the SEM image of the TiO_2 microspheres indicated the presence of a more uniform spherical morphology, with particle sizes predominantly in the 0.7–1.1 μm range. The significant difference in the particle sizes between Al_2O_3 and TiO_2 plays a crucial role in determining their optical scattering properties. Al_2O_3, which is in the sub-200 nm range, primarily scatters visible and short-wavelength NIR radiation, whereas TiO_2, with a size distribution centered around ~1 μm, extends scattering into the longer NIR region. It was expected that the combined effect of these scatterers in a heterogeneous bilayered structure would enhance broadband solar reflectance.

To evaluate the light scattering efficiency of Al_2O_3 and TiO_2, Mie scattering simulations were performed for varying particle sizes (Fig. 3). The scattering efficiency of the TiO_2 microspheres exhibited a strong size-dependent response (Fig. 3(a)), with particles in the range of 0.8–1 μm displaying broadband scattering in the NIR region (700–2500 nm), making them highly effective for radiative cooling applications. Similarly, Al_2O_3 particles with diameters of 50–300 nm demonstrated enhanced scattering in the visible and short-wavelength NIR range (400–1500 nm) (Fig. 3(b)). These results suggest that integrating both TiO_2 and Al_2O_3 into a bilayered or composite structure can enable it to effectively cover a wider solar spectrum, leading to enhanced broadband solar reflectance and improved cooling performance. The solar reflectance of the fabricated PVDF-HFP-TiO_2, PVDF-HFP-Al_2O_3, PVDF-HFP-TiO_2-Al_2O_3, and PVDF-HFP-TiO_2/Al_2O_3 nanofibers is presented in Fig. 3(c). All samples exhibited high reflectance across the solar spectrum (300–2500 nm), with the average reflectance exceeding 90%, demonstrating their excellent potential for passive radiative cooling. Notably, the pure PVDF-HFP-Al_2O_3, bilayered PVDF-HFP-TiO_2/Al_2O_3 membranes achieved a similarly high average reflectance (~95%), while mixed PVDF-HFP-TiO_2-Al_2O_3 (91%), PVDF-HFP-TiO_2 membrane had slightly lower reflectance (~90%) due to their UV absorption. The PVDF-HFP-TiO_2-Al_2O_3 samples exhibited characteristic UV absorption below 400 nm due to the inherent bandgap properties of TiO_2, which contrasts with the high UV reflectance observed in the pure PVDF-HFP-Al_2O_3 sample. The mixed composition was designed with a 10 : 10 weight ratio of TiO_2 and Al_2O_3 to maintain the total particle loading at 20 wt% while ensuring balanced contributions from both scattering components. Alternative ratios such as 5 : 15 or 15 : 5 would shift the composition toward single-component behavior, negating the synergistic spectral complementarity that the equal 10 : 10 ratio provides. This difference in performance was in accordance with the Mie scattering analysis (Fig. 3(a) and (b)), where the Al_2O_3 microspheres (50–300 nm) demonstrated superior scattering efficiency in the visible region (400–700 nm), while the TiO_2 microspheres (0.7–1.1 μm) provided effective scattering in the near-infrared region (700–2500 nm). The thermal emissivity spectra validate the cooling potential of all nanofiber membranes (Fig. 3(d)), with each

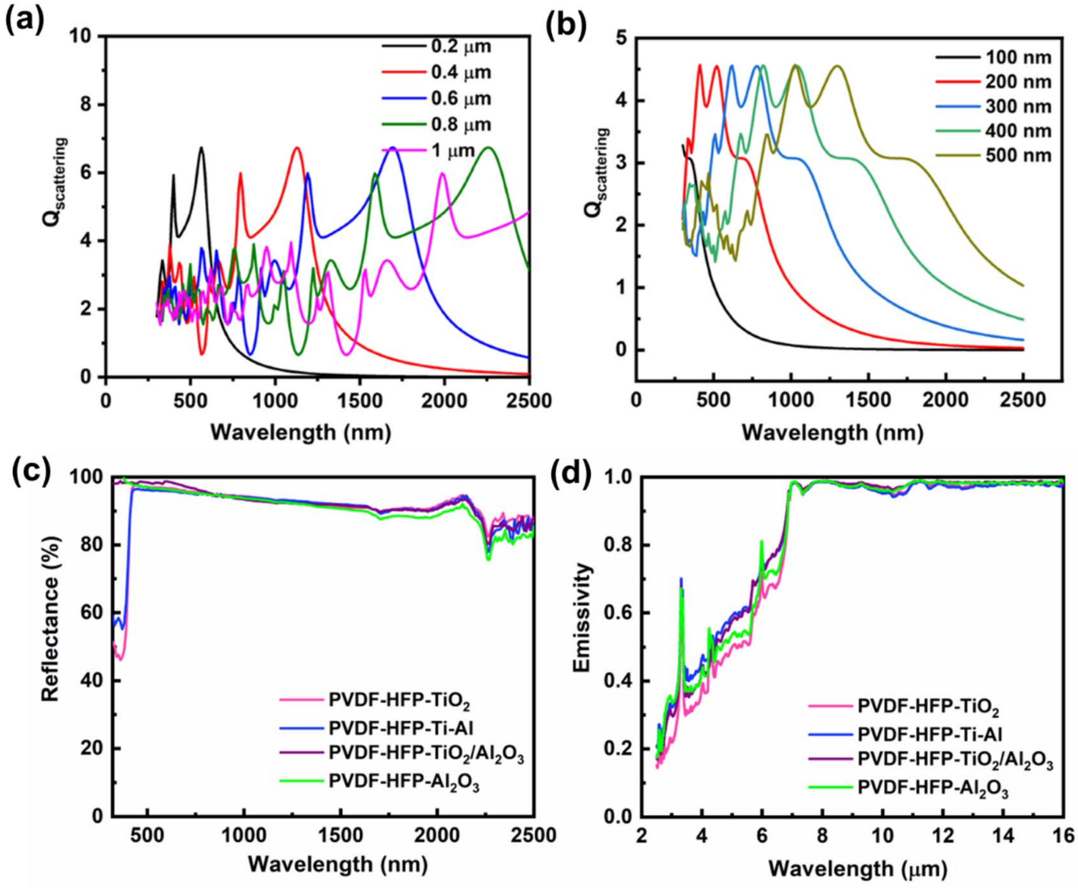

Fig. 3 Electromagnetic scattering efficiency of (a) TiO_2 microspheres, and (b) Al_2O_3 microspheres. (c) UV-vis-NIR reflectance and (d) thermal emissivity plots of the PVDF-HFP-TiO_2, PVDF-HFP-Al_2O_3, PVDF-HFP-TiO_2-Al_2O_3, and PVDF-HFP-TiO_2/Al_2O_3 nanofibers.

sample exhibiting strong emissivity (~0.98) in the atmospheric transparency window (8–13 μm), ensuring efficient thermal radiation to outer space. The consistently high emissivity across all samples confirmed that the PVDF-HFP polymer matrix effectively contributed to infrared emission through its C–F vibrational modes, regardless of the particle composition.[34,35]

3.3 Outdoor radiative cooling performance

The outdoor radiative cooling performance of the prepared nanofiber samples was evaluated on July 30, 2024, from 11:00 AM to 6:00 PM under hot summer conditions in Gwangju, South Korea. The measurement setup consisted of cavities covered with the nanofiber samples, with the variation in temperature recorded using a multichannel thermocouple system. Wind speed and humidity data were collected simultaneously. The measurements were conducted with a PE shield covering the device to assess its impact on cooling performance. Fig. 4(a)–(d) present the radiative cooling performance of the PVDF-HFP-TiO_2, PVDF-HFP-Al_2O_3, PVDF-HFP-TiO_2-Al_2O_3, and PVDF-HFP-TiO_2/Al_2O_3 nanofiber membranes under outdoor conditions on July 30, 2024. At peak solar intensity (Fig. S6), the PE shielded air temperature reached ~55 °C, while the temperatures of all the nanofiber covered samples were significantly lower.

The bilayered PVDF-HFP-TiO_2/Al_2O_3 structure exhibited the lowest temperature, followed by PVDF-HFP-TiO_2-Al2O3, PVDF-HFP-Al_2O_3, and PVDF-HFP-TiO_2. All of the nanofiber samples exhibited lower temperatures compared to the PE shielded air temperature, confirming their radiative cooling ability. PVDF-HFP-TiO_2/Al_2O_3 achieved the lowest peak temperature, highlighting its superior solar reflectance and thermal emissivity. Fig. 4(b) presents the temperature difference (ΔT) between the samples and the PE shielded air temperature. PVDF-HFP-TiO_2/Al_2O_3 demonstrated the most significant cooling effect, with its ΔT reaching approximately 12 °C. The PVDF-HFP-Al_2O_3, PVDF-HFP-TiO_2-Al_2O_3 and PVDF-HFP-TiO_2 nanofibers also exhibited cooling effects, albeit with smaller ΔT values (approximately 9 ° C, 10 °C, and 8 °C, respectively). The bilayered PVDF-HFP-TiO_2/Al_2O_3 structure thus optimally balanced solar reflectance and IR emission, achieving maximum cooling.

The theoretical net radiative cooling power was calculated using a mid-latitude summer atmospheric model ($T_{\text{ambient}} = 27$ °C, RH = 40%) to validate the experimental cooling performance. Under daytime conditions ($I_{\text{solar}} = 1000$ W m^{-2}), the bilayered PVDF-HFP-TiO_2/Al_2O_3 membrane demonstrated a maximum theoretical cooling power of 139.5 W m^{-2}, which increased to 189.5 W m^{-2} during the night due to the elimination of solar heat input. At the experimentally achieved

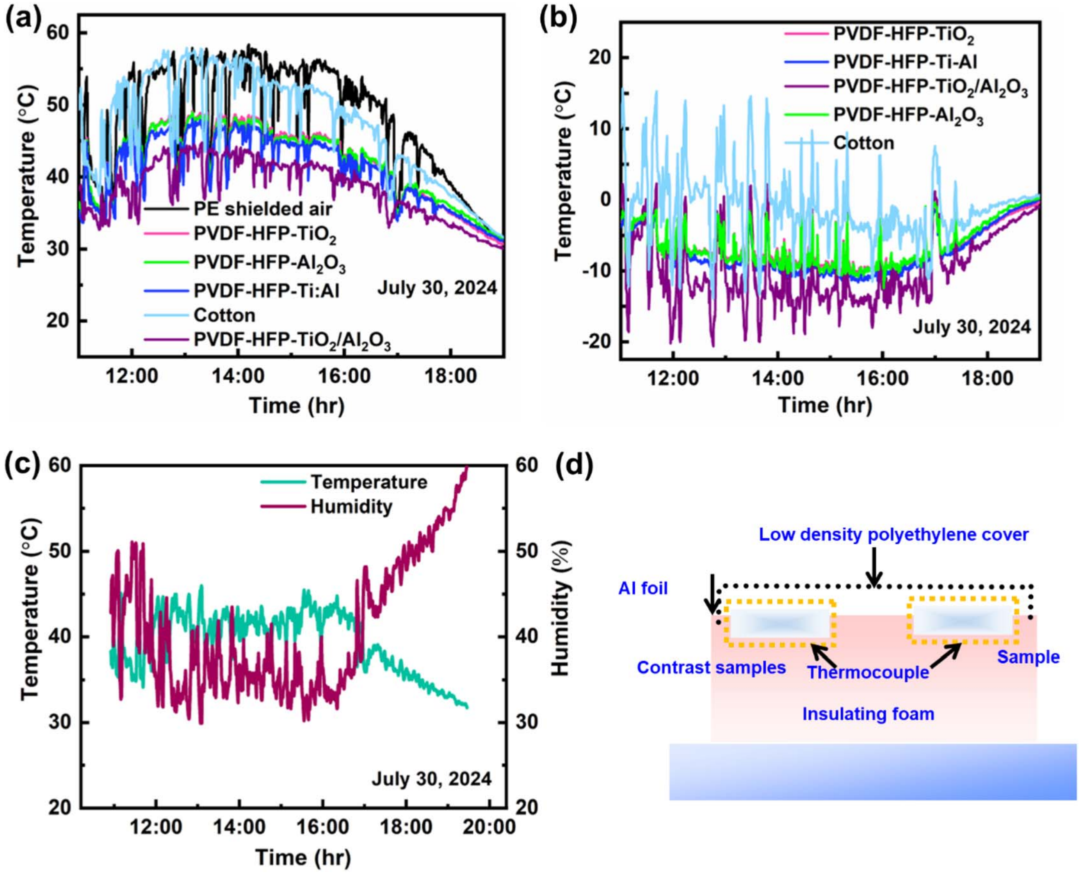

Fig. 4 Outdoor radiative cooling performance results measured on July 30, 2024. (a) Real-time temperature curves for the samples recorded with a PE shield, (b) cooling capacity of the samples measured using a PE shield, (c) ambient temperature and humidity levels recorded on July 30, 2024, and (d) schematic of the passive daytime radiative cooling (PDRC) device setup.

temperature difference of 12 °C, the theoretical cooling power was 71.7 W m^{-2} during the daytime and 121.7 W m^{-2} at night, validating the observed cooling performance (Fig. S7). Table S1 compares previously reported radiative cooling capacities with those achieved by the samples in the present study. Fig. 4(c) shows the variations in temperature and humidity during the experiment. The humidity level fluctuated between 30% and 50%, while the temperature closely followed the solar intensity cycle. The nanofiber membranes maintained radiative cooling even under fluctuating humidity levels, demonstrating their reliability for real world applications.

3.4 Testing the applicability of PVDF-HFP-TiO$_2$/Al$_2$O$_3$ nanofibers

The experimental results indicated that the PVDF-HFP-TiO$_2$/Al$_2$O$_3$ nanofiber fabric had the potential to be a highly effective radiative cooling layer for buildings and vehicles. To demonstrate its performance, we applied the nanofiber fabric to a house model and conducted an outdoor passive radiative cooling test on August 28, 2024, in Gwangju, South Korea (Fig. 5(a)–(d)). The PVDF-HFP-TiO$_2$/Al$_2$O$_3$ nanofiber fabric achieved a 6.2 °C lower temperature than the unprotected house model under peak summer noon conditions (Fig. 5(a)). For real-world outdoor applications, radiative cooling nanofibers must also exhibit excellent mechanical durability. The mechanical properties of the PVDF-HFP-TiO$_2$, PVDF-HFP-TiO$_2$-Al$_2$O$_3$, and PVDF-HFP-TiO$_2$/Al$_2$O$_3$ nanofiber membranes are summarized in Fig. 5(e). Of these membranes, PVDF-HFP-TiO$_2$-Al$_2$O$_3$ demonstrated the highest tensile strength (6.4 MPa) and stiffness (Young's modulus: 12.3 MPa), making it the strongest and most rigid material. In contrast, PVDF-HFP-TiO$_2$ had the greatest elongation at break (180.65%), highlighting its superior ductility and stretchability. The bilayered PVDF-HFP-TiO$_2$/Al$_2$O$_3$ nanofiber structure exhibited the lowest tensile strength (3.2 MPa) and stiffness (Young's modulus: 2.7 MPa), yet it maintained a balance between flexibility and mechanical integrity. Additionally, the PVDF-HFP-TiO$_2$/Al$_2$O$_3$ nanofibers exhibited inherent hydrophobicity due to their polymer matrix and interwoven fibrous sphere surface features (Fig. 5(f) and S8). The surface of the fabric thus allowed for the easy removal of accumulated dirt through simple water treatment (Fig. S9). Overall, the PVDF-HFP-TiO$_2$/Al$_2$O$_3$ nanofibers offer strong solar reflectance, high thermal emissivity, excellent water resistance, and a well-balanced combination of strength and flexibility, making them a promising candidate for radiative cooling applications.

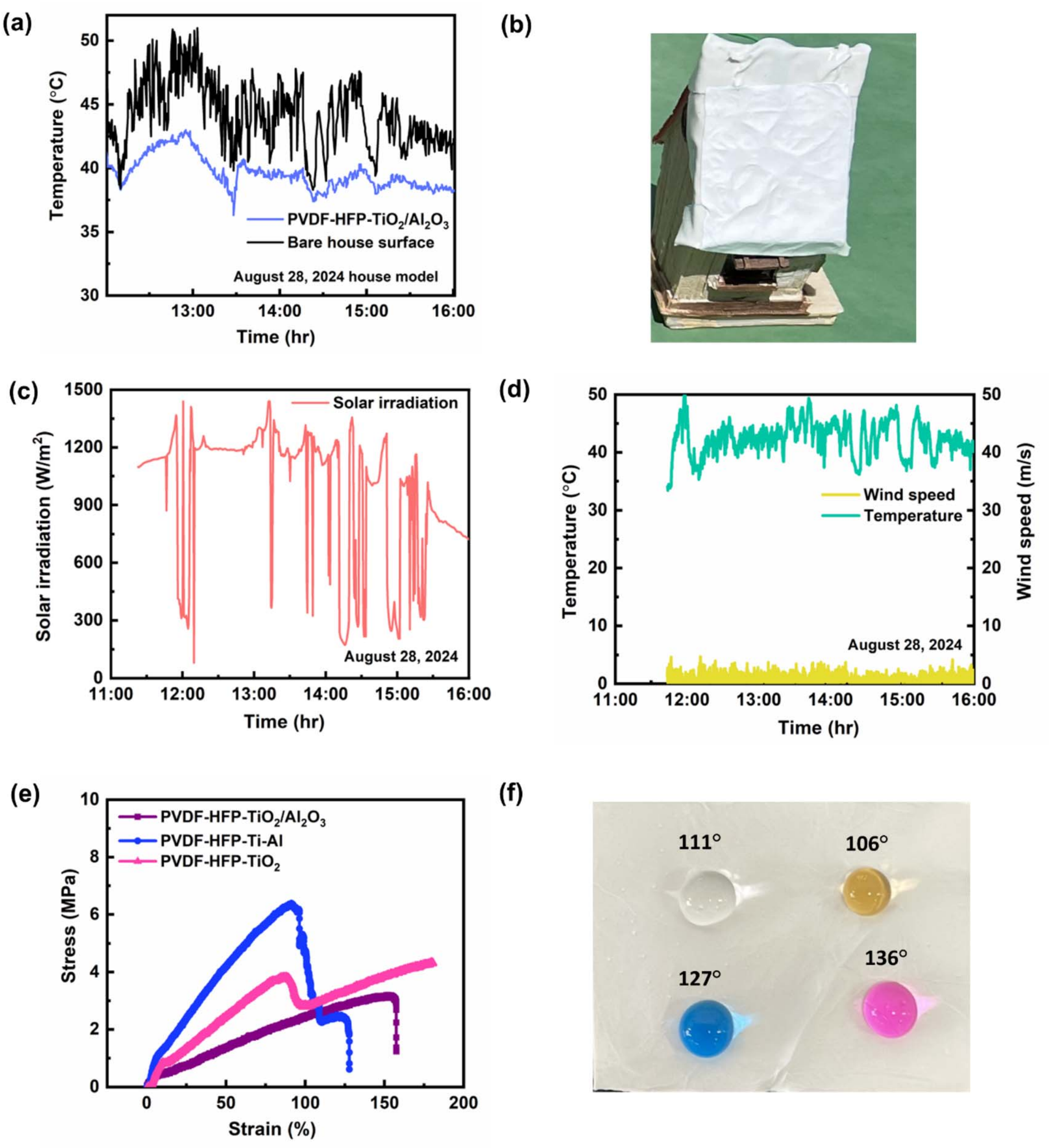

Fig. 5 Outdoor radiative cooling performance results measured on August 28, 2024. (a) Real-time temperature curves for the samples recorded with a house model. (b) Picture of the house model. (c) Solar irradiation spectrum measured on August 28, 2024. (d) Ambient temperature and wind speed levels recorded on August 28, 2024. (e) Mechanical properties of the prepared samples. (f) PVDF-HFP-TiO_2/Al_2O_3 nanofiber fabric with liquid droplets on its surface.

4. Conclusion

By systematically comparing four PVDF-HFP-based membrane designs, this study demonstrated that architectural design plays a crucial role in optimizing passive radiative cooling performance. While all samples exhibited excellent optical properties (>90% solar reflectance, ∼98% thermal emissivity), the bilayered PVDF-HFP-TiO_2/Al_2O_3 structure achieved superior cooling performance (temperature reduction of 12 °C) compared to single-component (TiO_2: 8 °C, Al_2O_3: 9 °C) and mixed composite (10 °C) designs. This performance enhancement demonstrates that strategic layer segregation and particle size optimization are as important as individual material properties for maximizing radiative cooling efficiency. The incorporation of complementary TiO_2 and Al_2O_3 microspheres enhanced solar reflectance through synergistic Mie scattering effects, with theoretical calculations (cooling power of 71.7 W m^{-2} during the daytime and 121.7 W m^{-2} at night) validating the experimental observations. The bilayered architecture facilitates optimal spectral coverage while minimizing particle interference, representing a significant advancement in passive cooling material design.

Conflicts of interest

There are no conflicts to declare.

Data availability

The data supporting this article have been included as part of the SI.

The supplementary information file contains detailed information on materials characterization, theoretical calculations, and outdoor PDRC measurements. It also includes size distribution plots, FE-SEM and EDX mapping images, the solar irradiation spectrum, theoretical radiative cooling power plots, water contact angle images, soil dust removal images, and radiative cooling performance comparison table with previously reported radiative cooling membranes. See DOI: **https://doi.org/10.1039/d5ta04422g**.

Acknowledgements

This work was supported by the National Research Foundation of Korea (NRF) grant funded by the Korea government (MSIT) (RS-2024-00357288) and the Basic Science Research Program through the National Research Foundation of Korea (NRF) funded by the Ministry of Education (NRF-2022R1I1A1A01062898).

References

1 J. Mandal, Y. Yang, N. Yu and A. P. Raman, Paints as a scalable and effective radiative cooling technology for buildings, *Joule*, 2020, **4**, 1350–1356.

2 X. Yu, J. Chan and C. Chen, Review of radiative cooling materials: performance evaluation and design approaches, *Nano Energy*, 2021, **88**, 106259.

3 N. Cheng, Z. Wang, Y. Lin, X. Li, Y. Zhang, C. Ding, C. Wang, J. Tan, F. Sun, X. Wang, J. Yu and B. Ding, Breathable dual-mode leather like nanotextile for efficient day time radiative cooling and heating, *Adv. Mater.*, 2024, **36**, 2403223.

4 S. Y. Heo, G. J. Lee and Y. M. Song, Heat shedding with photonic structures: radiative cooling and its potential, *J. Mater. Chem. C*, 2022, **10**, 9915–9937.

5 Q. Ye, X. Chen, H. Yan and M. Chen, Thermal conductive radiative cooling film for local heat dissipation, *Mater. Today. Phys.*, 2025, **50**, 101626.

6 S. Liu, F. Zhang, X. Chen, H. Yan, W. Chen and M. Chen, Thin paints for durable and scalable radiative cooling, *J. Energy Chem.*, 2024, **90**, 176–182.

7 R. Yu, M. Wang, W. Lu, J. Wang, Y. Cao, Y. Yang, W. Wang and J. Wang, Infrared ultralow-emissivity polymeric metafabric conductors enabling remarkable electromagnetic and thermal management, *Adv. Funct. Mater.*, 2025, **35**, 2421347.

8 S. Feng, L. Yao, M. Feng, H. Cai, X. He, M. He, X. Bu and Y. Zhou, Regeneration of pea-pod-like cellulose acetate fibers as aerogel-derived boards for building thermal regulation and carbon reduction, *Adv. Fiber Mater.*, 2024, **6**, 570–582.

9 W. Hu, F. Zhang, X. Tan, Y. Tu and S. Nie, Antibacterial PVDF coral-like hierarchical structure composite film fabrication for self-cleaning and radiative cooling effect, *ACS Appl. Mater. Interfaces*, 2024, **16**, 19828–19837.

10 L. An, J. Ma, P. Wang, A. Kuchmizhak, J. Yao, H. Xu and W. Wang, In situ switchable nanofiber films based on photoselective asymmetric assembly towards year-round energy saving, *J. Mater. Chem. A*, 2024, **12**, 18304–18312.

11 H. Ma, L. Wang, S. Dou, H. Zhao, M. Huang, Z. Xu, X. Zhang, X. Xu, A. Zhang, H. Yue, G. Ali, C. Zhang, W. Zhou, Y. Li, Y. Zhan and C. Huang, Flexible daytime radiative cooling enhanced by enabling three-phase composites with scattering interfaces between silica microspheres and hierarchical porous coatings, *ACS Appl. Mater. Interfaces*, 2021, **12**, 19282–19290.

12 Y. Lin, C. Qin, Z. Liang, W. Lin, J. Wang and D. Li, Biomimetic structurally colored film for high-performance radiative cooling, *Adv. Opt. Mater.*, 2024, **12**, 2401020.

13 X. Li, Z. Zhang, X. Zhang, Y. Cao, Y. Yang, W. Wang and J. Wang, A polymer nanocomposite with strong full-spectrum solar absorption and infrared emission for all-day thermal energy management and conversion, *Adv. Sci.*, 2024, **11**, 2308200.

14 W. Wei, Y. Zhu, Q. Li, Z. Cheng, Y. Yao, Q. Zhao, P. Zhang, X. Liu, Z. Chen, F. Xu and Y. Gao, An Al_2O_3-cellulose acetate-coated textile for human body cooling, *Sol. Energy Mater. Sol. Cells*, 2020, **211**, 110525.

15 G. Qi, X. Tan, Y. Tu, X. Yang, Y. Qiao, Y. Wang, J. Geng, S. Yao and X. Chen, Ordered-porous-array polymethyl methacrylate films for radiative cooling, *ACS Appl. Mater. Interfaces*, 2022, **14**, 31277–31284.

16 Q. Yue, L. Zhang, C. He, B. Liu, W. Wang, Z. Lu, G. Liu and X. Gao, Polymer composites with hierarchical architecture and dielectric particles for efficient daytime subambient radiative cooling, *J. Mater. Chem. A*, 2023, **11**, 3126–3135.

17 Y. Zhai, Y. Ma, S. N. David, D. Zhao, R. Lou, G. Tan, R. Yang and X. Yin, Scalable-manufactured randomized glass-polymer hybrid metamaterial for daytime radiative cooling, *Science*, 2017, **355**, 1062–1066.

18 S. Atiganyanun, J. B. Plumley, S. J. Han, K. Hsu, J. Cytrynbaum and T. L. Peng, Effective radiative cooling by paint-format microsphere-based photonic random media, *ACS Photonics*, 2018, **5**, 1181–1187.

19 X. Xue, M. Qiu, Y. Li, Q. M. Zhang, S. Li and Z. Yang, Creating an eco-friendly building coating with smart subambient radiative cooling, *Adv. Mater.*, 2020, **32**, e1906751.

20 X. Wang, X. Liu, Z. Li, H. Zhang, Z. Yang and H. Zhou, Scalable flexible hybrid membranes with photonic structures for daytime radiative cooling, *Adv. Funct. Mater.*, 2020, **30**, 1907562.

21 C. Zhou, C. Fu, G. Tian, F. He, S. Huang and Z. Guo, Biomimetic alumina film for passive daytime radiative cooling, *ACS Appl. Mater. Interfaces*, 2024, **16**, 70737–70745.

22 J. Yun, D. Chae, S. So, H. Lim, J. Noh, J. Park, N. Kim, C. Park, H. Lee and J. Rho, Optimally designed multi-material microparticle-polymer composite paints for passive daytime radiative cooling, *ACS Photonics*, 2023, **10**, 2608–2617.

23 D. Chae, S. Son, H. Lim, P. H. Jung, J. Ha and H. Lee, Scalable and paint-format microparticle–polymer composite enabling high-performance daytime radiative cooling, *Mater. Today Phys.*, 2021, **18**, 100389.

24 J. Huang, M. Li and D. Fan, Core-shell particles for devising high-performance full-day radiative cooling paint, *Appl. Mater. Today*, 2021, **25**, 101209.

25 L. Du, Z. Zhou, J. Li, B. Hu, C. Wang, J. Zheng, W. Liu, R. Li and W. Chen, Highly efficient subambient all-day passive radiative cooling textiles with optically responsive MgO embedded in porous cellulose acetate polymer, *Chem. Eng. J.*, 2023, **469**, 143765.

26 X. Mei, T. Wang, Y. Zhang, T. Huang, M. Chen and L. Wu, Scalable bilayer thin coatings with enhanced thermal dissipation for passive daytime radiative cooling, *Chem. Eng. J.*, 2024, **495**, 153182.

27 J. Hou, H. Zhang, J. Lin, X. Qiu, W. Zhao, Y. Xiang, H. Zhang, G. Xing, D. Zheng, G. Li and Z. Tang, Hollow TiO_2 sub microspheres assembled by tiny nanocrystals as superior anode for lithium-ion battery, *J. Mater. Chem. A*, 2019, **7**, 23733–23738.

28 N. Cheng, D. Miao, C. Wang, Y. Lin, A. A. Babar, X. Wang, Z. Wang, J. Yu and B. Ding, Nanosphere-structured hierarchically porous PVDF-HFP fabric for passive daytime radiative cooling *via* one-step water vapor-induced phase separation, *Chem. Eng. J.*, 2023, **460**, 141581.

29 J. Zhu, Z. An, A. Zhang, Y. Du, X. Zhou, Y. Geng and G. Chen, Anisotropic porous designed polymer coatings for high-performance passive all-day radiative cooling, *iScience*, 2022, **25**, 104126.

30 A. Aili, Z. Wei, Y. Chen, D. Zhao, R. Yang and X. Yin, Selection of polymers with functional groups for daytime radiative cooling, *Mater. Today Phys.*, 2019, **10**, 100127.

31 C. Xue, R. Wei, X. J. Guo, B. Y. Liu, M. Du, M. C. Huang, H. G. Li and S. T. Jia, Fabrication of superhydrophobic P(VDF-HFP)/SiO2 composite film for stable radiative cooling, *Comp. Sci. Technol.*, 2022, **220**, 109279.

32 D. Thiyagarajan, S. Li, S. Subramani, A. Thirumurugan and B. K. Lee, Titanium metal–organic framework-derived nanocrystalline TiO_2-supported nitrogen-doped carbon nanostructures as highly efficient antibiotic adsorbents, *Appl. Surf. Sci.*, 2024, **645**, 158842.

33 B. Deng, P. A. Advincula, D. X. Luong, J. Zhou, B. Zhang, Z. Wang, E. A. McHugh, J. Chen, R. A. Carter, C. Kittrell, J. Luo, Y. Zhao, B. I. Yakobson, Y. Zhao and J. M. Tour, High-surface-area corundum nanoparticles by resistive hotspot-induced phase transformation, *Nat. Commun.*, 2022, **13**, 5027.

34 S. Yoon, J. Seo, J. Jung, M. Choi, B. J. Lee and J. B. Kim, Improving radiative cooling performance *via* strong solar reflection by dense Al_2O_3 particles in a polymeric film, *Int. J. Heat Mass Transf.*, 2024, **227**, 125574.

35 J. W. Cho, Y. Lee, J. H. Kim, R. Hu, E. Lee and S. H. Kim, Directional radiative cooling *via* exceptional epsilon-based microcavities, *ACS Nano*, 2023, **17**, 10442–10451.